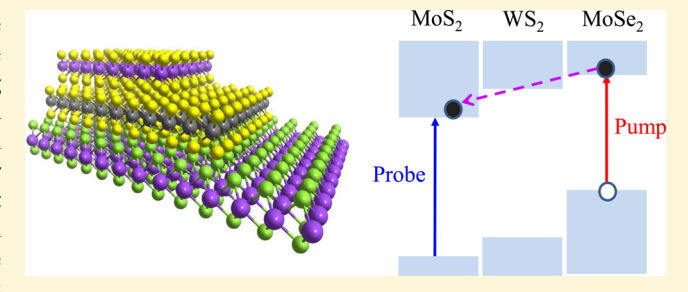


# Highly Efficient and Anomalous Charge Transfer in van der Waals **Trilayer Semiconductors**

Frank Ceballos, Ming-Gang Ju, Samuel D. Lane, Xiao Cheng Zeng, And Hui Zhao And Hui Zhao Khang Zeng, Samuel D. Lane, Xiao Cheng Zeng, Samuel D. Lane, Xiao Cheng Zeng, Xiao Chen

Supporting Information

ABSTRACT: Two-dimensional materials, such as graphene and monolayer transition metal dichalcogenides, allow the fabrication of multilayer structures without lattice matching restriction. A central issue in developing such artificial materials is to understand and control the interlayer electron transfer process, which plays a key role in harnessing their emergent properties. Recent photoluminescence and transient absorption measurements revealed that the electron transfer in heterobilayers occurs on ultrafast time scales. However, there is still a lack of fundamental understanding on how this



process can be so efficient at van der Waals interfaces. Here we show evidence suggesting the coherent nature of such interlayer electron transfer. In a trilayer of MoS<sub>2</sub>-WS<sub>2</sub>-MoSe<sub>2</sub>, electrons excited in MoSe<sub>2</sub> transfer to MoS<sub>2</sub> in about one picosecond. Surprisingly, these electrons do not populate the middle WS<sub>2</sub> layer during this process. Calculations showed the coherent nature of the charge transfer and reproduced the measured electron transfer time. The hole transfer from MoS<sub>2</sub> to MoSe<sub>2</sub> is also found to be efficient and ultrafast. The separation of electrons and holes extends their lifetimes to more than one nanosecond, suggesting potential applications of such multilayer structures in optoelectronics.

KEYWORDS: van der Waals interface, transition metal dichalcogenide, charge transfer, coherent transport, transient absorption, two-dimensional material

he newly discovered two-dimensional materials with nanometer thicknesses, such as graphene and monolayer transition metal dichalcogenides, have shown promising electronic and optical properties.<sup>1–5</sup> In particular, they allow the fabrication of multilayer heterostructures without lattice matching restriction.<sup>5,6</sup> However, the van der Waals nature of the interlayer coupling could result in inefficient hoping-like interlayer electron transfer, hindering harnessing their emergent properties. Hence, understanding and controlling the interlayer electron transfer in van der Waals heterostructures is important for implementing these materials in logic electronics, thin-film transistors, and optoelectronics.

Recent efforts on this issue have focused on bilayer heterostructures. Steady-state optical measurements have revealed effective charge transfer between different monolayers from the quenching of photoluminescence.  $^{7-15}$  Later, transient absorption measurements were attempted to time resolve the charge transfer between two different monolayers. It was found that this process occurs on an ultrafast time scale that was beyond the time resolution of these studies. 16-19 Due to the weak interlayer coupling and the large momentum mismatch between these atomic layers, such a fast transfer is rather surprising.<sup>20</sup> Various mechanisms have been proposed, such as resonant transfer to higher energy states, 20 delocalization of the electron wave function in momentum space, 20 coherence

enhancement,<sup>21</sup> and Coulomb potential enhancement.<sup>22</sup> However, a full understanding is yet to be developed.

Here we show evidence on the coherent nature of interlayer charge transfer in a trilayer of MoS<sub>2</sub>-WS<sub>2</sub>-MoSe<sub>2</sub>. Electrons excited in MoSe<sub>2</sub> transfer to MoS<sub>2</sub>, without populating the middle WS<sub>2</sub> layer, in 1 ps at room temperature. Calculations showed the coherent nature of the charge transfer and reproduced the transfer time. The hole transfer from MoS<sub>2</sub> to MoSe<sub>2</sub> is also efficient and ultrafast. The separation of electrons and holes extends their lifetimes to 1 ns, suggesting potential applications of such multilayer structures in optoelectronics.

The trilayer sample, which is schematically shown in Figure 1a, was fabricated by mechanically exfoliating the monolayers and transferring them one by one, with the sequence of MoSe<sub>2</sub>-WS<sub>2</sub>-MoS<sub>2</sub>, on a silicon substrate covered with 90 nm of SiO2. The monolayer thickness of each layer was identified by optical contrast and photoluminescence. After transferring each monolayer, the sample was annealed at 200 °C for 2 h under a H<sub>2</sub>/Ar (20 sccm/100 sccm) environment at a pressure

Received: November 17, 2016 Revised: January 24, 2017 Published: February 17, 2017

Department of Physics and Astronomy, The University of Kansas, Lawrence, Kansas 66045, United States

<sup>&</sup>lt;sup>‡</sup>Department of Chemistry, University of Nebraska—Lincoln and Nebraska Center for Materials and Nanoscience, Lincoln, Nebraska 68588, United States

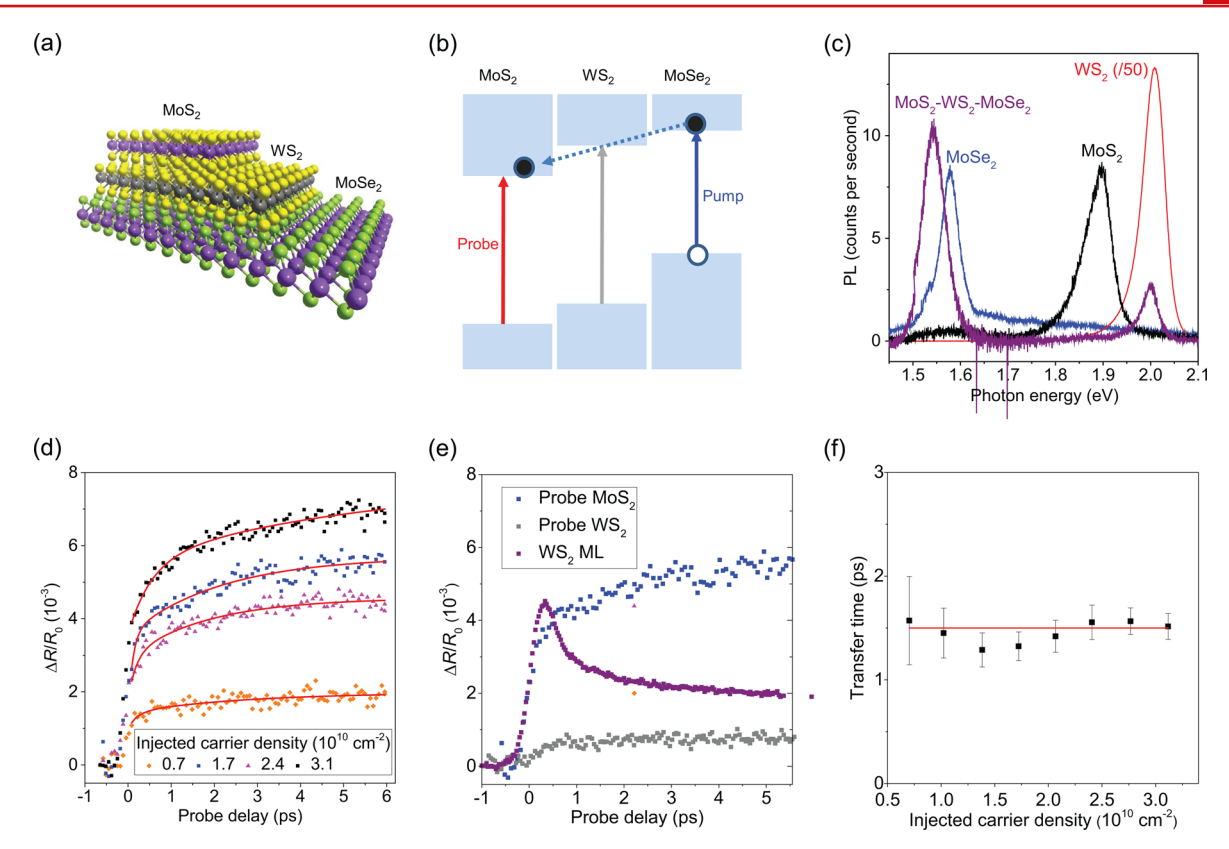


Figure 1. (a) Schematic illustration of the  $MoS_2-WS_2-MoSe_2$  trilayer sample studied. (b) Band alignment of the trilayer sample and the pump-probe configuration, where a pump pulse excited the  $MoSe_2$  layer and a probe pulse detects carriers in  $MoS_2$ . (c) Photoluminescence spectra of the trilayer (purple) and monolayers of  $MoS_2$  (black),  $WS_2$  (red, divided by 50), and  $MoSe_2$  (blue) under steady excitation of 405 nm and 0.5  $\mu$ W. (d) Differential reflection of a 1.88 eV probe pulse (sensing carriers in  $MoS_2$ ) after a pump pulse of 1.57 eV injected carriers in  $MoSe_2$ . The red curves are fits. (e) The gray symbols are differential reflection of a 2.00 eV probe (sensing  $WS_2$  of the trilayer) after a pump pulse of 1.57 eV injected carriers in  $MoSe_2$ . The purple symbols are measured from a  $WS_2$  monolayer sample with a 3.14 eV pump pulse injecting carriers. The blue symbols are replotted from (d) for comparison. (f) Charge transfer time as a function of injected carrier density.

of about 2 Torr. The sample was kept in an ambient condition during all the measurements.

According to first-principle calculations, 23,24 this trilayer forms a ladder alignment in both the conduction and the valence bands, as schematically shown in Figure 1b. The conduction band minimum and valence band maximum lie in the MoS<sub>2</sub> and MoSe<sub>2</sub> layers, respectively. Photoluminescence measurements were performed to probe the quality of the interfaces, as shown in Figure 1c. Without the interlayer charge transfer, the spectrum of the trilayer would resemble the sum of the spectra from the three monolayers. However, the WS<sub>2</sub> Aexciton peak is about 250 times weaker in the trilayer than the monolayer. The significant quenching of the MoS<sub>2</sub> and MoSe<sub>2</sub> peaks, which are practically invisible in the trilayer spectrum, also confirms the high quality of the interfaces between the monolayers.<sup>7-12</sup> The strong peak at 1.54 eV observed in the trilayer is consistent with the charge transfer exciton PL we previously identified in a MoSe<sub>2</sub>-WS<sub>2</sub> heterostructure.<sup>22</sup>

The interlayer charge transfer in the trilayer sample was studied by the ultrafast pump—probe technique based on a 80 MHz femtosecond laser system. A 1.57 eV and 100 fs pump pulse is used to selectively excite electrons in MoSe<sub>2</sub>. Since the optical bandgaps of MoS<sub>2</sub> and WS<sub>2</sub> are 1.88 and 2.01 eV, respectively, the pump photon energy is not sufficient to excite these layers. Once excited to the conduction band of MoSe<sub>2</sub>, the electrons are expected to transfer to MoS<sub>2</sub> (Figure 1b). To monitor the population of these electrons in the conduction

band of MoS2, the differential reflection of a 1.88 eV probe pulse (tuned to the MoS<sub>2</sub> optical bandgap) was measured as a function of its arrival time at the sample with respect to the pump pulse. Here, the differential reflection is defined as the normalized change of the probe reflection due to the pumpinjected carriers,  $\Delta R/R_0 = (R - R_0)/R_0$ . A few examples of the measured signal are shown in Figure 1d. The carrier densities initially injected in MoSe<sub>2</sub>, as indicated in the label of Figure 1d, were estimated from the fluences of the pump pulse and the absorption coefficient of MoSe<sub>2</sub> (Supporting Information). A control experiment performed with a MoSe<sub>2</sub> monolayer yielded no signal, confirming that the 1.88 eV probe does not sense carriers in MoSe<sub>2</sub>. Hence, the signal originates from electrons in MoS<sub>2</sub> that have transferred from MoSe<sub>2</sub>. The rise of the signal can be modeled, as indicated by the red curves in Figure 1d, by noticing that the population of electrons in MoS<sub>2</sub> should follow  $N(t) = N_0[1 - \exp(-t/\tau)]$ , where  $N_0$  is the initially injected density in  $MoSe_2$  and  $\tau$  the transfer time. From these fits and others that are not shown, we obtain an average charge transfer time of  $1.5 \pm 0.2$  ps, which shows no significant density dependence (Figure 1f).

To determine whether the electrons temporarily populate the conduction band of the WS<sub>2</sub> middle layer during the transfer, a 2.00 eV probe was used, which is tuned to the optical bandgap of WS<sub>2</sub>. To gauge the probe, we first measured a WS<sub>2</sub> monolayer sample. With a pump of 3.18 eV injecting a carrier density of about  $4.3 \times 10^{10}$  cm<sup>-2</sup>, a signal of about  $4 \times 10^{-3}$  was

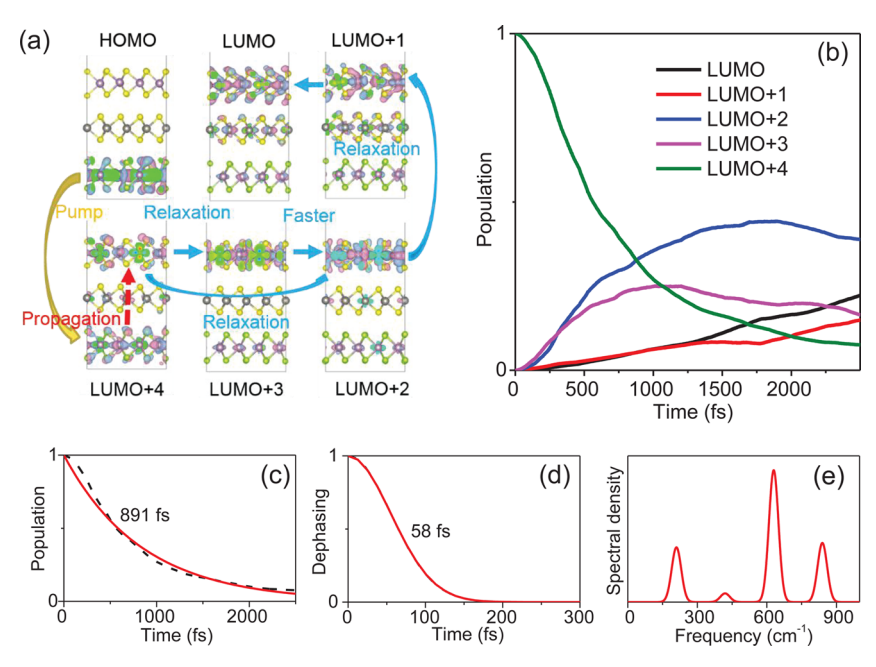


**Figure 2.** (a) Schematic diagram of energy levels involved in the excited electron dynamics. (b) Decay of population of excited electron states. (c) Decay of LUMO+4 population fitted by exponential,  $f(t) = \exp(-t/\tau)$ . (d) Pure-dephasing functions for the charge transfer between LUMO+4 and LUMO+3. The decay time scale represents the elastic electron—phonon scattering time, fitted by a Gaussian. (e) Fourier transformation of the energy gaps between the LUMO+4 and LUMO+3 for electron transfer.

observed (purple symbols in Figure 1e, more data can be found in Supporting Information, Figure S9). If the electron transfer from  $MoSe_2$  to  $MoS_2$  is an incoherent and sequential process, the electrons are expected to temporarily populate  $WS_2$ . With the 1.57 eV pump injecting a density of  $4.3 \times 10^{10}$  cm $^{-2}$  in  $MoSe_2$ , one would expect the detection of a transient signal that last for about 1 ps and with a peak magnitude similar to the purple symbols. However, the observed signal (open symbols) is much weaker than expected and does not show the temporal feature described above. A detailed investigation on the magnitude and temporal behavior of this residual signal shows that it originates from the holes residing in  $MoSe_2$  (Supporting Information, Figure S7).

The observation that the electrons do not populate WS2 as they move from MoSe<sub>2</sub> to MoS<sub>2</sub> suggests that the transfer could be a coherent process. To obtain physics insight into this process, we performed nonadiabatic molecular dynamics (NAMD) simulations.<sup>27,28</sup> The molecular structure of the trilayer system with 108 atoms per unit cell is shown in Figure 2a. Geometry optimization and adiabatic MD simulation were performed using the Quantum Espresso program<sup>29</sup> with the plane-wave basis, ultrasoft pseudopotential, and Perdew-Burke-Ernzerhof (PBE) exchange-corrleation functional. 30,31 The size of the plane-wave basis was chosen to satisfy the 40 Ry energy and 400 Ry charge density cutoffs. The dispersion correction was included via the semiempirical London terms (PBE-D).<sup>32</sup> The initially optimized structure was used as a starting point for the adiabatic MD simulation, where a 50 ps trajectory of the system was obtained with 1 fs steps. The Andersen thermostat was employed to control the temperature of the system at ambient conditions.<sup>33</sup>

To model the relaxation of the photoexcited electrons, it is important to adequately describe spontaneous transitions between different electronic states. NAMD implemented in the PYXID code<sup>27,28</sup> as an extension of MD with using fewest-switch surface hopping within the time-dependent Kohn–Sham

theory<sup>34</sup> can simulate such transitions well. The timedependent Schrödinger equation,  $i\hbar\partial|\Psi\rangle/\partial t = H|\Psi\rangle$ , was solved along the nuclear trajectory R(t). The transition probability between states  $|i\rangle$  and  $|j\rangle$  was then given by the time-dependent amplitudes  $\{c_i(t)\}\$  of a basis set representation in the total wave function,  $|\psi(t,R)\rangle = \sum_i c_i(t)|i(R)\rangle$ , and from the magnitude of the nonadiabatic coupling  $d_{ii} = \langle i|d/dt|j \rangle$ , which can be computed numerically using the approximation  $d_{ii}(t +$ dt)  $\approx 1/(2dt)[\langle i(t)|j(t+dt)\rangle - \langle i(t+dt)|j(t)\rangle]$ . The current simulations employed the adiabatic basis  $\{|i\rangle\}$ . A detailed discussion of NAMD methodology can be found elsewhere. 35,36 In our simulations, we assumed that the photogenerated electron-hole pairs rapidly dissociate so that we can neglect the electron-hole interaction. Computation of the latter requires significantly more demanding computational methods. Quantum decoherence effects were investigated using the optical response theory and a semiclassical correction to the NA dynamics.<sup>37</sup> The electronic structures of configurations taken from the MD trajectory were computed with only the  $\Gamma$  point. Here, a more accurate screened Coulomb hybrid functional HSE06 implemented in the Vienna ab Initio Simulation Package (VASP) was used to compute the electronic structures.

Figure 2a shows wave functions of the states near the band edges, based on the configuration of the MD trajectory at 1 ps. The highest occupied molecular orbital (HOMO) is entirely localized in MoSe<sub>2</sub>, while the lowest unoccupied molecular orbital (LUMO) is mostly localized in MoS<sub>2</sub> but slightly extends to the other two layers. Among higher excited states, the LUMO+1, LUMO+2, and LUMO+3 states exhibit similar wave function distributions as LUMO, whereas only LUMO+4 shows significant distribution in the MoSe<sub>2</sub>. Hence, the 1.57 eV pump excites electrons initially from HOMO to LUMO+4, where the electrons are delocalized between MoSe<sub>2</sub> and MoS<sub>2</sub>. The initially excited LUMO+4 can be viewed as a donor state while the four lower LUMO states can be viewed as acceptor

states. The strong donor—acceptor interaction results in the electron transfer from MoSe<sub>2</sub> to MoS<sub>2</sub>. More importantly, in both acceptor and donor states, molecular orbitals are mostly localized in MoSe<sub>2</sub> and MoS<sub>2</sub>, indicating that electrons can coherently transfer from MoSe<sub>2</sub> to MoS<sub>2</sub> without populating WS<sub>2</sub>. Results of more accurate computations based on the HSE06 functional, particularly the electronic structure computation for configurations at different time in the trajectory, reaffirm the computational results (Supporting Information, Figures S1–S4).

Figure 2b shows the simulated dynamics of the electron population at various LUMO levels. From an exponential fit (Figure 2c), an electron transfer time of about 0.9 ps was obtained, in good agreement with the experiment. In particular, the time evolution of the population indicates that the initially excited state (LUMO+4) relaxes to LUMO+3 due to the electron transfer between LUMO+3 and LUMO+4. To quantitatively characterize the phonon-induced loss of electronic coherence, the pure-dephasing functions for charge transfer from LUMO+4 to LUMO+3 are plotted in Figure 2d, and the computed decay time is about 58 fs from the Gaussian fitting. Compared with the decay time for charge transfer from LUMO+4 to LUMO+2, the loss of coherence between LUMO +4 and LUMO+3 is slower (Supporting Information, Figure S5). The longer coherence results in faster electron dynamics between LUMO+4 and LUMO+3, suggesting electrons in LUMO+4 relax to LUMO+3 first, then to LUMO+2. The much longer decay time for LUMO+3 to LUMO+2 further supports this sequence of relaxation process (Supporting Information, Figure S6). In any event, because the LUMO+3 and LUMO+2 states have little distribution in WS<sub>2</sub>, the middle WS<sub>2</sub> layer is never populated during the charge relaxation process, which is again consistent with the experiment.

To reveal the charge transfer promoted by phonons, Figure 2e shows the computed spectral density obtained from Fourier transformation of the energy difference between LUMO+4 and LUMO+3. The phonons involved in the LUMO+4-to-LUMO +3 process have higher frequencies, compared with those in LUMO+4-to-LUMO+2 and LUMO+3-to-LUMO+2. Specifically, the LUMO+4-to-LUMO+3 charge transer process is coupled with phonons with 210, 625, and 835 cm<sup>-1</sup> frequencies (particularly with the 625 cm<sup>-1</sup>), whereas the LUMO+4-to-LUMO+2 and LUMO+3-to -LUMO+2 processes are mainly coupled with the phonons of 415 cm<sup>-1</sup>. Clearly, phonons with higher frequencies cause stronger nonadiabatic coupling and lead to faster charge transfer from LUMO+4 to LUMO+3.<sup>39</sup>

The ladder arrangement of the valence bands in the sample allows hole transfer from MoS2 to MoSe2, opposite to the electron transfer direction. To study this process, a 1.88 eV pump excites MoS<sub>2</sub> while a 1.57 eV probe monitors MoSe<sub>2</sub>. The result is shown by the blue symbols in Figure 3a. Although undesired for the sake of investigating hole transfer, the pump also inevitably injects carriers in MoSe2, which has a smaller optical bandgap. The total carrier density injected in the two layers is about  $1.3 \times 10^{11}$  cm<sup>-2</sup>. To isolate the contribution of the holes directly injected in MoSe<sub>2</sub>, we changed the pump to 1.75 eV, so that it injects carriers in MoSe<sub>2</sub> only, with a density of about  $4.4 \times 10^{10}$  cm<sup>-2</sup>. It is not energetic enough to excite MoS<sub>2</sub>. As the excited electrons transfer to MoS<sub>2</sub>, the signal observed (red symbols in Figure 3a) is induced by holes in MoSe<sub>2</sub>. Since the signal is proportional to the hole density, we can deduce the signal corresponding to a hole density of 1.3 × 10<sup>11</sup> cm<sup>-2</sup> by multiplying the observed signal with a factor of 3.

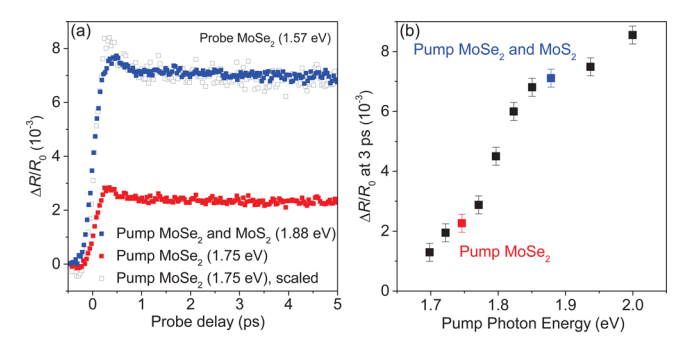


**Figure 3.** (a) Differential reflection signal of the 1.57 eV probe after the trilayer sample is pumped by 1.88 (blue) and 1.75 eV (red) pumps, respectively. (b) Differential reflection signal at a probe delay of 3 ps as a function of the pump photon energy. The two data points corresponding to panel a are plotted with the corresponding colors.

The result (gray symbols) is in excellent agreement with blue symbols. This comparison confirms that holes injected in  $MoS_2$  transfer to  $MoSe_2$  with a near unity efficiency. This interpretation is further confirmed by the systematic variation of the signal measured at 3 ps as the pump photon energy is changed, shown in Figure 3b. Since the temporal profiles of the two signals are identical, both rising to maximum on a time scale limited by the time resolution of the instrument, the hole transfer process is at least as fast as the instrument response time of 0.3 ps (Supporting Information, Figure S8) and is faster than the electron transfer.

After the charge transfer, the electrons and holes settle in different layers and are separated by a middle layer, which is expected to extend the carrier lifetime. To probe the lifetime of the electrons in  $MoS_2$  after their transfer from  $MoSe_2$ , the differential reflection of the 1.88 eV probe was measured over a long time range after the 1.57 eV pump injected a carrier density of  $1.1 \times 10^{10}$  cm<sup>-2</sup> in  $MoSe_2$ . As shown by the blue symbols in Figure 4a, the lifetime of these electrons is about 950 ps. This is significantly longer than the 30 ps photocarrier lifetime in  $MoS_2$  monolayer (open symbols), determined by measuring a monolayer  $MoS_2$  sample with the same probe but a 3.14 eV pump. We also probed the lifetime of holes in  $MoSe_2$ 

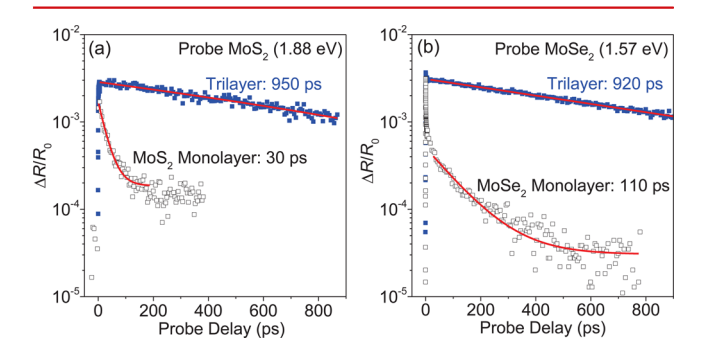


**Figure 4.** (a) Blue solid symbols show the differential reflection of a 1.88 eV probe after a 1.57 eV pump pulse injected carriers with a peak density of  $1.1 \times 10^{10} \ \text{cm}^{-2}$  in the MoSe<sub>2</sub> layer of the trilayer sample. Open symbols represent results from a MoS<sub>2</sub> monolayer, with the same probe, but with a 3.14 eV pump pulse that injects carriers with the same density. The red curves are exponential fits. (b) The differential reflection of a 1.57 eV probe after a 2.00 eV pump pulse injected carriers in the trilayer (blue solid symbols) and a MoSe<sub>2</sub> monolayer (open symbols) with a density of  $9.5 \times 10^{10} \ \text{cm}^{-2}$ . The red curves are exponential fits.

by using the 1.57 eV probe. As shown in Figure 4b, the lifetime is also significantly extended compared to MoSe<sub>2</sub> monolayer and is reasonably consistent with the lifetime of electrons in MoS<sub>2</sub> of the trilayer (Supporting Information, Figure S9).

In summary, we time-resolved the transfer of electrons from MoSe<sub>2</sub> to MoS<sub>2</sub> monolayers that are separated by a WS<sub>2</sub> monolayer. The transfer time is about 1.5 ps. Considering the thickness of these monolayers of about 1 nm, such a transfer time corresponds to a speed on the order of 1000 m s<sup>-1</sup>. Surprisingly, the electrons do not populate the middle WS<sub>2</sub> layer during the transfer, which suggests that the transfer could be a coherent process. Our first-principle calculations reproduced both the transfer time and the coherent nature of the transfer. However, we note that our measurement does not directly monitor the coherence of the transfer due to the incoherent nature of the probe technique. We also observed efficient and ultrafast transfer of holes from MoS<sub>2</sub> to MoSe<sub>2</sub>. The spatial separation of electrons and holes by the WS<sub>2</sub> layer enhanced their lifetime to about 1 ns. These results on efficient charge transfer and long carrier lifetime suggest potential applications of van der Waals multilayers as new electronic and optoelectronic materials.

### ASSOCIATED CONTENT

# **S** Supporting Information

The Supporting Information is available free of charge on the ACS Publications website at DOI: 10.1021/acs.nano-lett.6b04815.

Sample fabrication, pump—probe measurements, estimation of pump-injected carrier density, and figures (PDF)

#### AUTHOR INFORMATION

# **Corresponding Authors**

\*E-mail: xzeng1@unl.edu. \*E-mail: huizhao@ku.edu.

#### ORCID

Xiao Cheng Zeng: 0000-0003-4672-8585 Hui Zhao: 0000-0003-4552-3836

# **Author Contributions**

F.C. and M.-G.J. contributed equally to this work.

#### Notes

The authors declare no competing financial interest.

# ACKNOWLEDGMENTS

H.Z. was supported by the National Science Foundation of USA under Grant Nos. DMR-1505852 and IIA-1430493. X.C.Z. was supported by the National Science Foundation of USA through the Nebraska Materials Research Science and Engineering Center (MRSEC) (grant no. DMR-1420645) and by the Nebraska Center for Energy Sciences Research in University of Nebraska—Lincoln. The computation was carried out at the Holland Computing Center and on NC3 computers in the Department of Chemistry at University of Nebraska—Lincoln.

#### REFERENCES

- (1) Novoselov, K. S.; Geim, A. K.; Morozov, S. V.; Jiang, D.; Zhang, Y.; Dubonos, S. V.; Grigorieva, I. V.; Firsov, A. A. Science **2004**, 306, 666–669
- (2) Wang, Q. H.; Kalantar-Zadeh, K.; Kis, A.; Coleman, J. N.; Strano, M. S. Nat. Nanotechnol. **2012**, *7*, 699–712.
- (3) Franklin, A. D. Science 2015, 349, aab2750.

- (4) Radisavljevic, B.; Radenovic, A.; Brivio, J.; Giacometti, V.; Kis, A. *Nat. Nanotechnol.* **2011**, *6*, 147–150.
- (5) Geim, A. K.; Grigorieva, I. V. Nature 2013, 499, 419-425.
- (6) Zhang, W.; Wang, Q.; Chen, Y.; Wang, Z.; Wee, A. T. S. 2D Mater. 2016, 3, 022001.
- (7) Fang, H.; Battaglia, C.; Carraro, C.; Nemsak, S.; Ozdol, B.; Kang, J. S.; Bechtel, H. A.; Desai, S. B.; Kronast, F.; Unal, A. A.; et al. *Proc. Natl. Acad. Sci. U. S. A.* **2014**, *111*, 6198–6202.
- (8) Lee, C. H.; Lee, G. H.; van der Zande, A. M.; Chen, W.; Li, Y.; Han, M.; Cui, X.; Arefe, G.; Nuckolls, C.; Heinz, T. F.; et al. *Nat. Nanotechnol.* **2014**, *9*, 676–681.
- (9) Furchi, M. M.; Pospischil, A.; Libisch, F.; Burgdorfer, J.; Mueller, T. *Nano Lett.* **2014**, *14*, 4785–4791.
- (10) Tongay, S.; Fan, W.; Kang, J.; Park, J.; Koldemir, U.; Suh, J.; Narang, D. S.; Liu, K.; Ji, J.; Li, J.; Sinclair, R.; Wu, J. *Nano Lett.* **2014**, *14*, 3185–3190.
- (11) Bellus, M. Z.; Ceballos, F.; Chiu, H.-Y.; Zhao, H. ACS Nano 2015, 9, 6459-6464.
- (12) Rivera, P.; Schaibley, J. R.; Jones, A. M.; Ross, J. S.; Wu, S.; Aivazian, G.; Klement, P.; Seyler, K.; Clark, G.; Ghimire, N. J.; Yan, J.; Mandrus, D. G.; Yao, W.; Xu, X. Nat. Commun. 2015, 6, 6242.
- (13) Loan, P. T.; Zhang, W.; Lin, C. T.; Wei, K. H.; Li, L. J.; Chen, C. H. Adv. Mater. 2014, 26, 4838-44.
- (14) Shih, C. J.; Wang, Q. H.; Son, Y.; Jin, Z.; Blankschtein, D.; Strano, M. S. ACS Nano 2014, 8, 5790-5798.
- (15) Azizi, A.; Eichfeld, S.; Geschwind, G.; Zhang, K.; Jiang, B.; Mukherjee, D.; Hossain, L.; Piasecki, A. F.; Kabius, B.; Robinson, J. A.; Alem, N. ACS Nano 2015, 9, 4882–4890.
- (16) Hong, X.; Kim, J.; Shi, S. F.; Zhang, Y.; Jin, C.; Sun, Y.; Tongay, S.; Wu, J.; Zhang, Y.; Wang, F. Nat. Nanotechnol. 2014, 9, 682–686.
- (17) Ceballos, F.; Bellus, M. Z.; Chiu, H. Y.; Zhao, H. ACS Nano 2014, 8, 12717-12724.
- (18) He, J.; Kumar, N.; Bellus, M. Z.; Chiu, H. Y.; He, D.; Wang, Y.; Zhao, H. Nat. Commun. 2014, 5, 5622.
- (19) Peng, B.; Yu, G.; Liu, X.; Liu, B.; Liang, X.; Bi, L.; Deng, L.; Sum, T. C.; Loh, K. P. 2D Mater. **2016**, 3, 025020.
- (20) Zhu, X.; Monahan, N. R.; Gong, Z.; Zhu, H.; Williams, K. W.; Nelson, C. A. J. Am. Chem. Soc. 2015, 137, 8313–8320.
- (21) Long, R.; Prezhdo, O. V. Nano Lett. 2016, 16, 1996-2003.
- (22) Wang, H.; Bang, J.; Sun, Y. Y.; Liang, L. B.; West, D.; Meunier, V.; Zhang, S. B. *Nat. Commun.* **2016**, *7*, 11504.
- (23) Guo, Y. Z.; Robertson, J. Appl. Phys. Lett. **2016**, 108, 233104.
- (24) Gong, C.; Zhang, H. J.; Wang, W. H.; Colombo, L.; Wallace, R. M.; Cho, K. J. Appl. Phys. Lett. 2013, 103, 053513.
- (25) Ceballos, F.; Bellus, M. Z.; Chiu, H. Y.; Zhao, H. Nanoscale **2015**, 7, 17523–17528.
- (26) Ceballos, F.; Zhao, H. Adv. Funct. Mater. 2016, 1604509.
- (27) Akimov, A. V.; Prezhdo, O. V. J. Chem. Theory Comput. 2014, 10, 789-804.
- (28) Akimov, A. V.; Prezhdo, O. V. J. Chem. Theory Comput. 2013, 9, 4959-4972.
- (29) Giannozzi, P.; Baroni, S.; Bonini, N.; Calandra, M.; Car, R.; Cavazzoni, C.; Ceresoli, D.; Chiarotti, G. L.; Cococcioni, M.; Dabo, I.; et al. *J. Phys.: Condens. Matter* **2009**, *21*, 395502.
- (30) Perdew, J. P.; Burke, K.; Ernzerhof, M. Phys. Rev. Lett. 1996, 77, 3865-3868
- (31) Perdew, J. P.; Burke, K.; Ernzerhof, M. Phys. Rev. Lett. 1997, 78, 1396–1396.
- (32) Grimme, S. J. Comput. Chem. 2006, 27, 1787-1799.
- (33) Andersen, H. C. J. Chem. Phys. 1980, 72, 2384-2393.
- (34) Tully, J. C. J. Chem. Phys. 1990, 93, 1061-1071.
- (35) Li, X.; Tully, J. C.; Schlegel, H. B.; Frisch, M. J. J. Chem. Phys. **2005**, 123, 084106.
- (36) Fischer, S. A.; Chapman, C. T.; Li, X. J. Chem. Phys. 2011, 135, 144102.
- (37) Habenicht, B. F.; Prezhdo, O. V. Phys. Rev. Lett. 2008, 100, 197402.
- (38) Kresse, G.; Furthmüller, J. Phys. Rev. B: Condens. Matter Mater. Phys. 1996, 54, 11169–11186.

(39) Long, R.; Guo, M.; Liu, L.; Fang, W. J. Phys. Chem. Lett. 2016, 7, 1830–1835.